eChem
https://www.sciltp.com/journals/eChem



Article

Ag Nanoparticle-Decorated $Co(OH)_2$ Nanowires for Efficient Electrocatalytic Nitrate Reduction to Ammonia

Lili Zhang [1], Yifan Li [1], Qian Bai [2], Runmin Li [1,2] and Huishan Shang [1,*]

[1] School of Chemical Engineering, Zhengzhou University, Zhengzhou 450001, China
[2] Energy & Catalysis Center, School of Materials Science and Engineering, Beijing Institute of Technology, Beijing 100081, China
* Correspondence: shanghs@zzu.edu.cn

How To Cite: Zhang, L.; Li, Y.; Bai, Q.; et al. Ag Nanoparticle-Decorated $Co(OH)_2$ Nanowires for Efficient Electrocatalytic Nitrate Reduction to Ammonia. *eChem* **2026**, *2*(2), 14. https://doi.org/10.53941/echem.2026.100014

Received: 13 October 2026
Revised: 5 November 2026
Accepted: 10 November 2026
Published: 20 November 2026

Abstract: Electrocatalytic nitrate reduction to ammonia (NO_3RR) provides a promising route for sustainable ammonia production under ambient conditions. However, the multi-step proton-coupled electron transfer process is often limited by the sluggish activation of NO_3^- and the subsequent hydrogenation of nitrogen-containing intermediates. Herein, Ag nanoparticles supported on $Co(OH)_2$ nanowires are constructed by an electrodepositing strategy, and the metal-support interaction is modulated to simultaneously optimize NO_3^- adsorption and water dissociation for achieving high energy efficiency at a range of potentials. *In Situ* characterization reveals that $Co(OH)_2$ promotes the initial reduction of NO_3^- to NO_2^-, whereas the uniformly distributed Ag nanoparticles enhance the formation of reactive hydrogen (*H), thereby accelerating the subsequent hydrogenation of nitrogen-containing intermediates. The resulting interfacial synergy significantly improves the overall NO_3RR kinetics and ammonia production. The $Ag/Co(OH)_2$ catalyst delivers an ammonia Faradaic efficiency of 96.35% at −0.4 V vs. RHE and maintains an FE above 80% over a broad potential range from 0.1 to −0.7 V vs. RHE. This work demonstrates an effective strategy for integrating nitrate activation and hydrogenation sites and provides mechanistic insights into the rational design of heterostructured catalysts for multi-step electrochemical reduction reactions.

Keywords: nitrate reduction; heterostructure; ammonia electrosynthesis; $Ag/Co(OH)_2$; Zn-NO_3^- battery

1. Introduction

Nitrogen is fundamental to modern industry and agriculture. The anthropogenic nitrogen cycle involves redox transformations among N_2, NH_3, and NO_x, exerting far-reaching effects on ecosystems and all life forms. However, excessive nitrogen fertilizer use in agriculture, together with NO_3^- accumulation in wastewater discharged from industrial activities, disrupts the nitrogen cycle and threatens human life and the global ecosystem [1–4]. Although various denitrification methods (e.g., landfill disposal and biological transformation) have been developed to treat NO_3^- rich wastewater, their high treatment costs and the potential for nitrate leakage remain major challenges. In this context, renewable-energy-driven electrocatalytic NO_3^- reduction reaction (NO_3RR) offers an environmentally benign route to upgrade NO_3^- into NH_3 [5–7]. Beyond enabling the sustainable treatment of NO_3^--rich wastewater, NO_3RR can also reduce the fossil fuel consumption and hydrocarbon dependence associated with Haber–Bosch ammonia production [8,9]. Despite its great potential, the practical application of NO_3RR is still hindered by its complex reaction pathway, which involves an eight-electron transfer process and multiple protonation steps [10–12]. The sluggish kinetics of intermediate conversion can result in the accumulation of toxic nitrite (NO_2^-) or poor ammonia selectivity [13,14]. In addition, the competing hydrogen evolution reaction (HER)

Copyright: © 2026 by the authors. This is an open access article under the terms and conditions of the Creative Commons Attribution (CC BY) license (https://creativecommons.org/licenses/by/4.0/).
Publisher's Note: Scilight stays neutral with regard to jurisdictional claims in published maps and institutional affiliations.

often becomes dominant in aqueous electrolytes, particularly at the highly negative potentials required to achieve high reaction rates, leading to a substantial decrease in Faradaic and energy efficiencies [15–17]. Therefore, developing electrocatalysts capable of suppressing HER while promoting the rapid hydrogenation of nitrogen-containing intermediates remains a major challenge.

The mechanism of nitrate electroreduction generally begins with NO_3^- adsorption at the active sites of the catalyst. It is worth noting that the adsorption affinity must be moderate; excessively strong adsorption induces active-site poisoning, whereas too weak adsorption impedes the subsequent reduction steps. The adsorption energy is governed by the electronic interaction between the electrocatalyst and NO_3^-. Therefore, tuning the electronic structure of the electrocatalyst is key to achieving suitable NO_3^- adsorption [18,19]. After NO_3^- adsorption, the NO_3RR pathway proceeds through nine consecutive hydrogenation steps. These steps require a continuous supply of active hydrogen (*H) [20]. In neutral and alkaline electrolytes, *H primarily originates from interfacial water dissociation. Water dissociation is kinetically sluggish and must overcome a high thermodynamic barrier. This limits *H supply and consequently affects the hydrogenation steps of NO_3RR at low overpotentials [21–23]. Rational regulation of the catalyst interfacial microenvironment can accelerate water dissociation kinetics and thereby promote the hydrogenation process in electrochemical NO_3RR. However, achieving synergistic optimization of NO_3^- adsorption and water dissociation through a single component remains challenging for catalyst design.

To address these kinetic limitations, transition-metal-based catalysts, such as Cu, Fe, Co, and Ti, have been extensively investigated owing to their tunable electronic structures and favorable binding with nitrogen-containing intermediates [24]. Among them, cobalt-based materials, including oxides [25], hydroxides [26], and phosphides [27,28], have shown considerable promise because of their ability to capture and activate nitrate ions. However, recent mechanistic studies indicate that monometallic Co catalysts often suffer from a kinetic mismatch. Although they exhibit strong nitrate adsorption, the generation of reactive hydrogen species is generally insufficient or sluggish, making it difficult to efficiently drive the rate-limiting hydrogenation step [29]. This can lead to nitrite accumulation and limited ammonia production. In contrast, noble metals, particularly Ag, possess high electrical conductivity and unique hydrogen adsorption kinetics, which can facilitate the regulation of the local proton environment [30,31]. Nevertheless, the high cost of noble metals and their tendency to promote the competing HER at high overpotentials limit their effectiveness when used alone. Therefore, constructing tandem interfaces or heterostructures [32,33] that integrate distinct active sites to decouple reactant adsorption from hydrogenation has emerged as a promising strategy for overcoming the intrinsic activity–selectivity constraints of single-component catalysts.

Herein, we report a high-performance $Ag/Co(OH)_2$ heterostructure catalyst constructed by electrodepositing Ag nanoparticles onto hydrothermally synthesized $Co(OH)_2$ nanowires. This architecture takes advantage of the distinct catalytic functions of the two components to accelerate the overall reaction kinetics. Through *in-situ* characterization and kinetic isotope effect analysis, we elucidate a synergistic reaction mechanism in which $Co(OH)_2$ nanowires primarily serve as nitrate adsorption sites and promote the initial conversion of NO_3^- to NO_2^-, whereas Ag nanoparticles facilitate the generation of reactive hydrogen, thereby accelerating the subsequent hydrogenation step, which is identified as a key kinetic bottleneck. Benefiting from this interfacial synergy, the optimized $Ag/Co(OH)_2$ catalyst achieves an ammonia Faradaic efficiency of 96.35% at a relatively low potential of −0.4 V vs. RHE and maintains an FE above 80% over a wide potential range from 0.1 to −0.7 V vs. RHE. This work highlights the importance of coordinating nitrate conversion and hydrogenation at complementary catalytic sites, offering a strategy for developing efficient electrocatalysts for nitrate-to-ammonia conversion.

2. Materials and Methods

2.1. Materials

$Co(NO_3)_2·6H_2O$ (99%) and NH_4F (96%) were purchased from Shanghai Macklin Biochemical Co., Ltd. (Shanghai, China). $CO(NH_2)_2$ (99.5%) and $AgNO_3$ (99.8%) were obtained from Shanghai Aladdin Biochemical Technology Co., Ltd. (Shanghai, China). KNO_3 (99%) and C_2H_5OH (99.7%) were supplied by Sinopharm Chemical Reagent Co., Ltd. (Shanghai, China). All chemical reagents were used without further purification.

2.2. Preparation of $Co(OH)_2$ Nanowires

$Co(OH)_2$ nanowires (NWs) were synthesized via a hydrothermal method. Typically, 0.875 g of $Co(NO_3)_2·6H_2O$, 0.360 g of $CO(NH_2)_2$, and 0.111 g of NH_4F were sequentially added to a beaker containing 30 mL of deionized water. The mixture was magnetically stirred at room temperature for 30 min. After the solid reagents were completely dissolved, a homogeneous, transparent, pink precursor solution was obtained. The resulting solution and pretreated

copper foam (CF) were then transferred into a 50 mL Teflon-lined stainless-steel autoclave, with the copper foam placed vertically. The autoclave was subsequently maintained at 120 °C for 6 h in a constant-temperature forced-air drying oven. After naturally cooling to room temperature, the autoclave was opened, and the copper foam electrode covered with light-purple $Co(OH)_2$ was collected. The electrode was repeatedly rinsed with deionized water and absolute ethanol and then dried in a vacuum oven at 60 °C for 12 h to obtain the $Co(OH)_2$ NWs.

2.3. Preparation of Ag/Co(OH)$_2$ NWs

Ag nanoparticles were uniformly deposited onto the surface of $Co(OH)_2$ NWs via an electrochemical deposition method. A conventional three-electrode electrochemical cell was employed, in which the as-prepared and dried $Co(OH)_2$ NWs served as the working electrode, a graphite rod was used as the counter electrode, and an Ag/AgCl electrode was employed as the reference electrode. The electrolyte consisted of 0.1 M KNO_3 containing 1 mg mL^{-1} $AgNO_3$. Electrochemical deposition was carried out at room temperature by applying a constant cathodic potential of −0.3 V to the working electrode using an electrochemical workstation. After deposition, the electrode was removed from the electrolyte, thoroughly rinsed with deionized water and ethanol, and dried to obtain the Ag/$Co(OH)_2$ NWs.

3. Results and Discussion

The Ag nanoparticles loaded on $Co(OH)_2$ were prepared through a two-step strategy of hydrothermal treatment and electrodeposition (Figure 1a). The obtained Ag/$Co(OH)_2$ heterostructure had a well-defined nanowire morphology. Typically, $Co(OH)_2$ nanowires were first directly grown on a Cu foam substrate by a hydrothermal process at 120 °C for 6 h using a Co precursor, NH_4F, and urea. Subsequently, Ag nanoparticles were uniformly deposited onto the $Co(OH)_2$ surface through controlled electrodeposition at a constant potential of −0.3 V. This hierarchical design of Ag/$Co(OH)_2$ heterostructure was intended to maximize the exposure of active sites while generating abundant interfacial regions for synergistic catalysis. Scanning electron microscopy (SEM) morphological characterization revealed that Ag/$Co(OH)_2$ forms a densely packed, radially arranged nanowire array with an average length of approximately 5~10 μm (Figure 1b). The morphologies of the corresponding control samples are presented in Figures S1 and S2. The Array nanowire configuration facilitated the rapid penetration and transmission of the electrolyte, which was conducive to accelerating the reaction process [34,35].

In addition, during the second step of electrodeposition, the duration of the process has a significant impact on the deposition amount and uniformity of the Ag nanoparticles. When the deposition time is short (<200 s), the surface of the $Co(OH)_2$ nanowires is relatively smooth with only a minimal amount of Ag nanoparticles adhered to it, indicating that the nucleation and growth of Ag have not yet been fully completed. The excessively low loading amount makes it difficult to provide sufficient catalytic active sites. When the deposition time is extended to 400 s (Figure S3), the Ag nanoparticles can be uniformly distributed and densely anchored onto the $Co(OH)_2$ nanowires. Following the electrodeposition process, transmission electron microscopy (TEM) images clearly demonstrated that Ag nanoparticles with a diameter of approximately 20 nm were densely and uniformly fixed on the surface of $Co(OH)_2$ nanowires (Figures 1c,d and S4). High-resolution transmission electron microscopy (HRTEM) further elucidated the crystal structure of silver, revealing distinct lattice fringes with a spacing of 0.24 nm, corresponding to the Ag (111) crystal plane (Figure 1e). The close contact observed between Ag and $Co(OH)_2$ was crucial for facilitating electron transfer and optimizing the adsorption energy of intermediates. Additionally, energy-dispersive X-ray spectroscopy (EDS) elemental mapping (Figure 1f) confirmed the uniform distribution of Ag, Co, and O elements throughout the nanowire structure, as well as the predominant presence of Ag nanoparticles on the surface.

The crystal structures of the as-prepared samples were characterized by X-ray diffraction (XRD). As shown in Figure 1g, the $Co(OH)_2$ sample exhibits no distinct diffraction peaks apart from the three characteristic peaks originating from the Cu substrate, indicating the predominantly amorphous nature of the $Co(OH)_2$ nanowires. After electrodeposition, two new diffraction peaks emerge, which can be assigned to the (111) and (200) planes of metallic Ag, respectively (PDF #04-016-6676). These results confirm the successful deposition of metallic Ag onto the $Co(OH)_2$ nanowire substrate. The XRD results were consistent with the TEM results. X-ray photoelectron spectroscopy (XPS) was then employed to investigate the surface chemical states of the catalysts. The survey spectrum showed characteristic signals corresponding to Cu, Co, O, and Ag (Figure S5). In the Co 2p spectrum (Figure 1h), two main peaks are observed at 781.0 (Co $2p_{3/2}$) and 797.1 eV (Co $2p_{1/2}$), accompanied by pronounced satellite peaks, which are characteristic of $Co(OH)_2$ in a hydroxide environment [36–38]. The Ag 3d spectrum (Figure 1i) displayed two peaks at 368.2 and 374.2 eV, which can be assigned to the Ag $3d_{5/2}$ and Ag $3d_{3/2}$ states of metallic Ag^0, respectively. The well-preserved chemical state of Ag together with the $Co(OH)_2$ support suggests

a strong electronic interaction between the two components, which may modulate the d-band center of the active sites and thereby enhance the intrinsic catalytic activity [39].

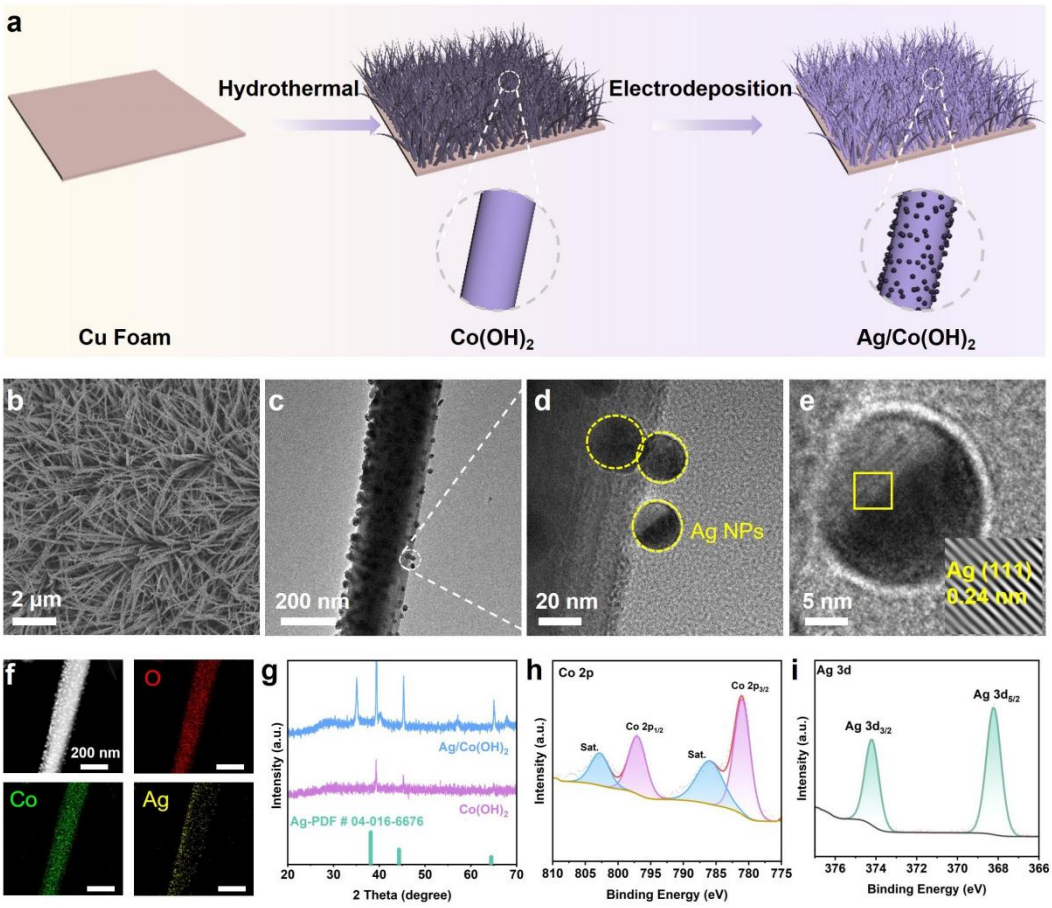

Figure 1. (**a**) Schematic illustration of the synthesis of Ag/Co(OH)$_2$. (**b**) SEM image. (**c**) TEM image. (**d**) Magnified TEM image showing the Ag nanoparticles (Ag NPs, yellow dashed circles) densely decorated on the Co(OH)$_2$ nanowire. (**e**) HRTEM image of a single Ag NP (the yellow box marks the measured region), with an interplanar spacing of 0.24 nm assigned to the Ag (111) plane (inset: corresponding FFT pattern). and (**f**) STEM image with the corresponding elemental mapping images of Ag/Co(OH)$_2$. (**g**) XRD patterns of Co(OH)$_2$ and Ag/Co(OH)$_2$. (**h**) Co 2p and (**i**) Ag 3d XPS spectra of Ag/Co(OH)$_2$.

The X-ray absorption near-edge structure (XANES) and extended X-ray absorption fine structure (EXAFS) spectroscopy were performed to elucidate the chemical states and local coordination environments of Ag and Co in Ag/Co(OH)$_2$. The normalized Ag K-edge XANES spectra were referenced against Ag foil, Ag_2O. respectively. The absorption edge position of Ag/Co(OH)$_2$ lies between that of metallic Ag foil and Ag_2O, and its white-line intensity is higher than that of Ag foil but lower than that of Ag_2O, demonstrating that the Ag in the sample comprises a mixture of mixed valence between 0 and +1 valence states (Figure 2a) [40]. In Figure 2b, the K_3-weighted Fourier-transformed EXAFS curves at the Ag K-edge reveal distinct characteristic signals attributable to the first-shell Ag-O coordination and Ag-Ag metallic bond scattering at approximately 1.5 Å and 2.7 Å, respectively, providing direct evidence that the Ag atoms coexist with metallic Ag nanoparticles within the sample [41]. To correlate the metal oxidation state with the XANES energy position, the first maximum of the first-derivative XANES spectra was determined for Ag/Co(OH)$_2$ and a series of reference compounds. In Figures 2c and S6, an oxidation state calibration curve was constructed using the absorption edge positions of Ag reference samples in different oxidation states. By applying this curve to the Ag/Co(OH)$_2$ sample, the average oxidation state of Ag was calculated to be 0.13, further quantitatively confirming the mixed-valence nature of the Ag species. In addition, from the XANES spectra in Figure 2d, the Co K-edge normalized XANES spectra were referenced against Co foil, CoO, and Co_2O_3. The Co absorption edge of Ag/Co(OH)$_2$ lies between those of CoO and Co_2O_3, indicating that the support Co exhibits a mixed valence state of Co^{2+}/Co^{3+}; the introduction of Ag species can alter the electronic structure of Co and modulate the Co^{2+}/Co^{3+} ratio [42]. The prominent signal at ~1.5 Å in the k^3-weighted Fourier-transformed EXAFS curve of the Co K-edge corresponds to the Co–O coordination shell, while the weak

signal in the high-R region is attributed to Co–Co coordination, consistent with the intrinsic coordination characteristics of the hydroxide cobalt oxide support (Figure 2e) [43]. Using the oxidation state calibration relationship established from the absorption edge of the Co standard sample, it was calculated that the average oxidation state of Co in $Ag/Co(OH)_2$ lies around 2.01 (Figures 2f and S7). The two-dimensional WT-EXAFS results for the Ag K-edge in Figure 2g–i reveal that the Ag foil exhibits a strong Ag–Ag scattering signal at k ≈ 9.0 $Å^{-1}$, while Ag_2O primarily displays Ag–O scattering at k ≈ 13.0 $Å^{-1}$ [44]. In contrast, $Ag/Co(OH)_2$ simultaneously exhibits both high-k Ag–O scattering and low-k Ag–Ag scattering signals, providing intuitive two-dimensional evidence of the coexistence of Ag single atoms and Ag nanoparticles. In the Co K-edge WT-EXAFS data shown in Figure 2j–l, the Co foil displays metallic Co–Co scattering, whereas CoO exhibits characteristic Co–O scattering features. The $Ag/Co(OH)_2$ is dominated by strong Co–O scattering, indicating that the Ag modification has not disrupted the primary Co–O coordination framework [45]. The collective XAFS results demonstrate that $Ag/Co(OH)_2$ contains Ag nanoparticles. During this process, electrons are transferred from Ag to the support, inducing valence state reconstruction at the Co sites [46]. This Ag–Co heterointerface and mixed-valence structure provide abundant active sites for nitrate reduction reactions, facilitating nitrate adsorption and multi-step proton–electron transfer processes. This structural foundation underpins the exceptional nitrate reduction performance of this catalyst.

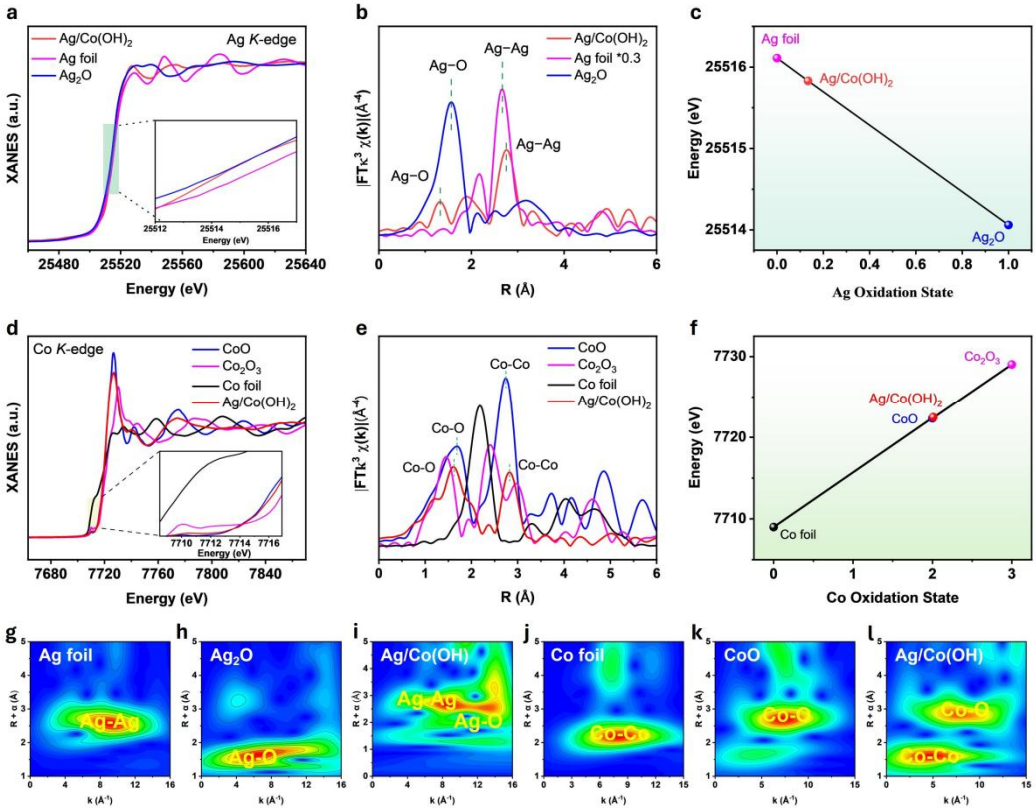

Figure 2. (**a**) Normalized Ag K-edge XANES spectra for $Ag/Co(OH)_2$, Ag foil, and Ag_2O. (**b**) Corresponding Fourier-transformed EXAFS curves; (**c**) Ag oxidation state calibration curve. (**d**) Normalized Co K-edge XANES spectra for $Ag/Co(OH)_2$, Co foil, CoO, and Co_2O_3. (**e**) Corresponding Fourier-transformed EXAFS curves. (**f**) Co oxidation state calibration curve. Wavelet transform (WT) contour plots: (**g**) Ag foil, (**h**) Ag_2O, and (**i**) $Ag/Co(OH)_2$. Co K-edge wavelet transform (WT) contour plots: (**j**) Co foil, (**k**) CoO, and (**l**) $Ag/Co(OH)_2$.

The electrocatalytic nitrate reduction reaction performance of $Ag/Co(OH)_2$ was evaluated in an alkaline electrolyte using a three-electrode H-type electrolytic cell (Figure 3a). A Pt plate was used as the anode, where the oxygen evolution reaction (OER) occurred, while the NO_3RR proceeded at the cathode. The self-supported $Ag/Co(OH)_2$ electrode grown on Cu foam served as the working electrode, with a Hg/HgO electrode used as the reference electrode. As shown by the linear sweep voltammetry (LSV) curves (Figure 3b), the introduction of nitrate resulted in a significant increase in current density for all catalysts compared with the nitrate-free electrolyte, confirming their catalytic activity toward NO_3RR. Notably, $Ag/Co(OH)_2$ exhibits substantially higher current densities across the entire potential window, indicating its superior catalytic activity in the nitrate-containing electrolyte. With increasing cathodic polarization, the current density of $Ag/Co(OH)_2$ reaches −650 mA

cm^{-2} at −0.7 V vs. RHE, significantly exceeding those of $Co(OH)_2$ and Ag/CF. Chronoamperometric measurements were further performed to evaluate the activity and selectivity of the catalysts. As shown in Figures 3c and S8, the ammonia Faradaic efficiency (FE) exhibits a volcano-shaped dependence on the applied potential, reaching a maximum value of 96.35% at approximately −0.4 V vs. RHE, together with a considerable ammonia yield. Meanwhile, the ammonia yield gradually increases with increasingly negative potentials and reaches approximately 56 mg at −0.7 V, nearly twice that obtained with $Co(OH)_2$. Notably, Ag/$Co(OH)_2$ maintains an ammonia FE above 80% within the low-overpotential range from 0.1 to −0.7 V vs. RHE, highlighting its effectiveness under relatively mild operating conditions. The catalyst also maintains a high FE over a broad range of nitrate concentrations, demonstrating its robust adaptability to different nitrate levels.

To further elucidate the superior NO_3RR performance of Ag/$Co(OH)_2$, the temporal evolution of nitrate consumption and the formation of nitrogen-containing reactants, intermediates, and products was monitored. The Ag/$Co(OH)_2$ system exhibits the fastest nitrate consumption rate, accompanied by minimal accumulation of the NO_2^- intermediate, further demonstrating its high selectivity toward ammonia (Figure 3d,e) [47]. To identify the nitrogen source of the produced ammonia, electrolysis experiments were conducted using isotopically labeled $^{15}NO_3^-$. The ^1H NMR spectrum of the resulting product shows the characteristic doublet associated with $^{15}NH_4^+$, rather than the triplet observed for $^{14}NH_4^+$, confirming that the produced ammonia originates exclusively from nitrate reduction (Figure 3f) [46]. To exclude potential interference from residual ammonia in the catalyst or external ammonia contamination, control experiments were conducted in the absence of nitrate and under open-circuit potential (OCP) conditions (Figure 3g). In both cases, negligible ammonia production was detected, further confirming the exclusive origin of the ammonia from nitrate reduction.

The long-term stability test (Figure 3h) shows negligible decay in both ammonia FE and yield during continuous operation for 10 h, demonstrating the excellent operational stability of the catalyst. Furthermore, comparison with representative NO_3RR catalysts (Figure 3i and Table S1) shows that Ag/$Co(OH)_2$ exhibits a competitive overall performance, delivering higher ammonia yield and FE at relatively low applied potentials. In electrocatalysis, the wettability of catalysts affects the interaction between the catalysts and electrolytes, which closely relates to their catalytic performance. The favorable hydrophilicity of the catalyst not only facilitates NO_3^- mass transport and permeation, thereby enabling the concurrent realization of high current density and high Faradaic efficiency (Figures S9 and S10). To examine the structural stability of the catalyst after electrolysis, Ag/$Co(OH)_2$ was characterized by X-ray diffraction, Scanning Electron Microscopy, transmission electron microscopy, and X-ray photoelectron spectroscopy. High-resolution TEM images reveal that the nanowire morphology is well preserved after the reaction, with no obvious aggregation of Ag nanoparticles (Figures S12–S15), and ICP shows that the Ag content slightly decreases from 20.0 wt% to 19.6 wt%, while the Co content changes from 48.0 wt% to 47.5 wt%, indicating the good structural stability of the heterostructure during NO_3RR.

To further elucidate the catalytic mechanism of the Ag/$Co(OH)_2$ heterostructure, a series of reaction kinetic analyses were performed. The electrochemically active surface area (ECSA) was estimated from the double-layer capacitance (C_{dl}) measurements (Figures 4a and S11). Ag/$Co(OH)_2$ exhibits a substantially higher C_{dl} value of 35.7 mF cm^{-2} than those of $Co(OH)_2$ (15.3 mF cm^{-2}) and Ag/CF (13.0 mF cm^{-2}), indicating that the hierarchical nanowire structure provides more exposed electrochemically active sites. This enhanced catalytic activity is further supported by the Tafel plots (Figure 4b), where Ag/$Co(OH)_2$ shows the lowest Tafel slope of 90.2 mV dec^{-1}, much lower than that of $Co(OH)_2$ (244.7 mV dec^{-1}), suggesting more favorable reaction kinetics. Based on the reaction kinetics, the rate constants (k_1 and k_2) for the conversion of NO_3^- to NO_2^- and NO_2^- to NH_3, respectively, were further evaluated for each catalyst (Figure 4c) [48]. For the first step ($NO_3^- \rightarrow NO_2^-$), $Co(OH)_2$ exhibits the highest rate constant ($k_1 = 4.13 \times 10^{-3}$ min^{-1}), followed by Ag/$Co(OH)_2$ ($k_1 = 3.84 \times 10^{-3}$ min^{-1}) and Ag ($k_1 = 2.62 \times 10^{-3}$ min^{-1}). In contrast, a markedly different trend is observed for the second step ($NO_2^- \rightarrow NH_3$). Although $Co(OH)_2$ exhibits a relatively high k_1, its k_2 is the lowest among the three catalysts, suggesting that NO_3^- can be rapidly reduced to NO_2^-, followed by the release and accumulation of NO_2^- in the electrolyte. This behavior is consistent with the relatively high NO_2^- FE observed for $Co(OH)_2$. For Ag/$Co(OH)_2$, NO_2^- intermediates are preferentially generated on the Co-based sites, while the adjacent Ag sites provide a locally H-rich environment that promotes the subsequent hydrogenation of NO_2^- [49]. The relatively high k_2/k_1 ratios of Ag and Ag/$Co(OH)_2$ compared with $Co(OH)_2$ indicate that Ag provides favorable sites for reactive hydrogen generation, allowing nitrogen-containing intermediates to rapidly consume *H and undergo further hydrogenation [50]. This synergistic effect accounts for their high selectivity toward NH_3 formation. Therefore, the enhanced NO_3RR activity of Ag/$Co(OH)_2$ can be reasonably attributed to the synergistic catalytic interaction between Ag and $Co(OH)_2$ sites. In this process, Ag facilitates water dissociation and the generation of reactive hydrogen species in the alkaline electrolyte, which can subsequently transfer to the nitrogen-containing intermediates adsorbed on nearby $Co(OH)_2$ sites. This promotes the further reduction of the relatively stable nitrite intermediate and ultimately favors NH_3 formation [51].

To further clarify the origin of the different NO_3RR performances, nitrite reduction reaction (NO_2RR) measurements were conducted to investigate the conversion of the NO_2^- intermediate. As shown by the LSV curves (Figure 4d), all catalysts exhibit substantially higher current densities in the NO_2^--containing electrolyte than in the blank electrolyte at the same potential, confirming their enhanced electrochemical activity toward NO_2RR. Among them, $Ag/Co(OH)_2$ shows the most pronounced increase in current density, indicating its superior ability to promote the further reduction of nitrogen-containing intermediates. As shown in Figure 4e,f, $Ag/Co(OH)_2$ delivers a higher NH_3 yield and Faradaic efficiency than $Co(OH)_2$. This performance difference suggests that $Co(OH)_2$ may suffer from the accumulation of reaction intermediates during NO_2^- reduction, resulting in sluggish reaction kinetics and the formation of undesired byproducts. The enhanced NO_2RR activity of $Ag/Co(OH)_2$ further supports its superior NO_3RR performance and validates the rationality of the heterostructure design. Notably, all catalysts exhibit Faradaic efficiencies above 90% for NO_2RR, indicating their high selectivity toward NH_3 formation from NO_2^-. In particular, $Ag/Co(OH)_2$ achieves an NO_2RR Faradaic efficiency of approximately 98.6% at −0.3 V vs. RHE, consistent with its excellent NO_3RR performance. We investigated the performance of electrocatalytic NH_3 synthesis under varying nitrate ion concentrations (ranging from 1 mM to 100 mM) to explore its potential applications. Figure 4g shows the LSV curves of $Ag/Co(OH)_2$ at different nitrate ion concentrations in 1 M KOH solution. At the same applied potential, the current density of the catalyst increased as the nitrate ion concentration increased, indicating that the NH_3 generation rate also increased with rising nitrate ion concentration. Figure 4h,i demonstrate the NO_3RR performance of $Ag/Co(OH)_2$ at various nitrate ion concentrations. The activity of the NO_3RR catalyst is directly influenced by the electrolyte concentration. The $Ag/Co(OH)_2$ composite exhibited similar Faradaic efficiencies at nitrate ion concentrations of 50 mM and 100 mM; however, when the nitrate ion concentration was below 10 mM, the Faradaic efficiency began to decrease.

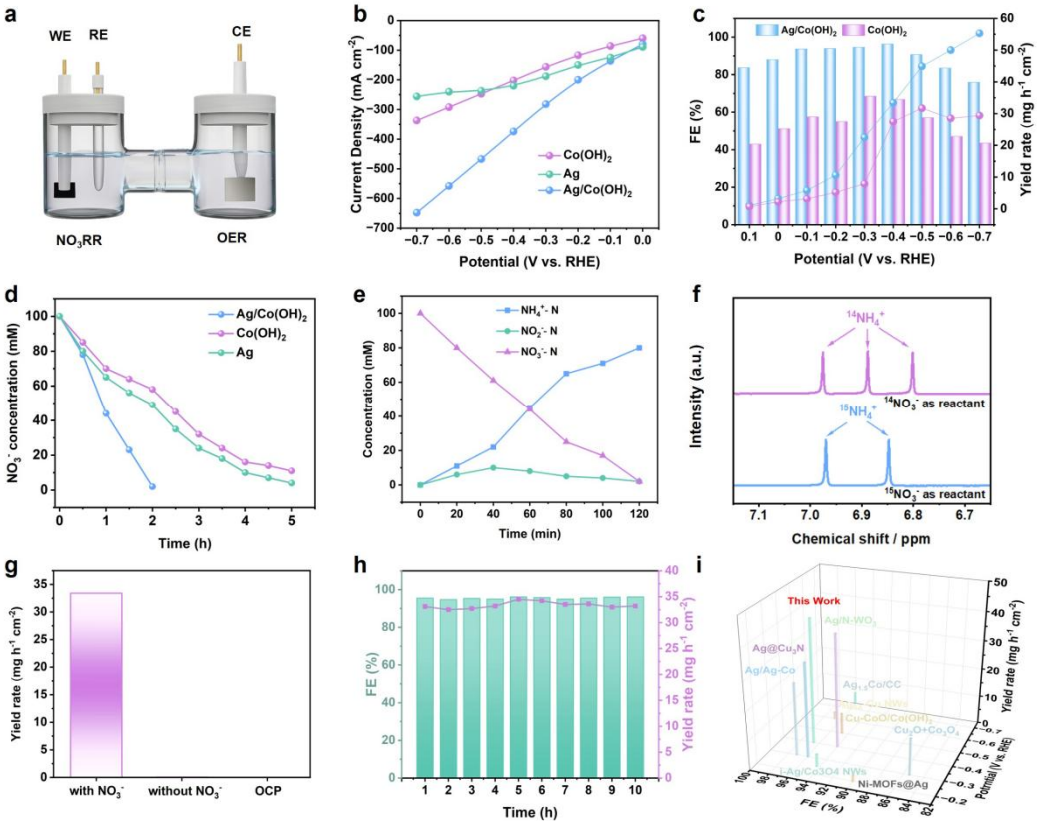

Figure 3. (**a**) Schematic illustration of the three-electrode H-type electrolytic cell. (**b**) LSV curves of Ag, $Co(OH)_2$, and $Ag/Co(OH)_2$. (**c**) Comparison of ammonia yield and Faradaic efficiency of $Ag/Co(OH)_2$ and $Co(OH)_2$ at different applied potentials. (**d**) Variation of NO_3^- concentration with reaction time. (**e**) Time-dependent evolution of nitrogen-containing species during NO_3RR. (**f**) ^1H NMR spectra of the electrolytes after NO_3RR using different nitrogen sources. (**g**) The ammonia production rate of the catalyst under different conditions. (**h**) NH_3 FEs and yield rates during 10 periods of 1 h continuous stability measurement over $Ag/Co(OH)_2$. (**i**) Comparison of ammonia yield and Faraday efficiency under different control conditions for various catalysts.

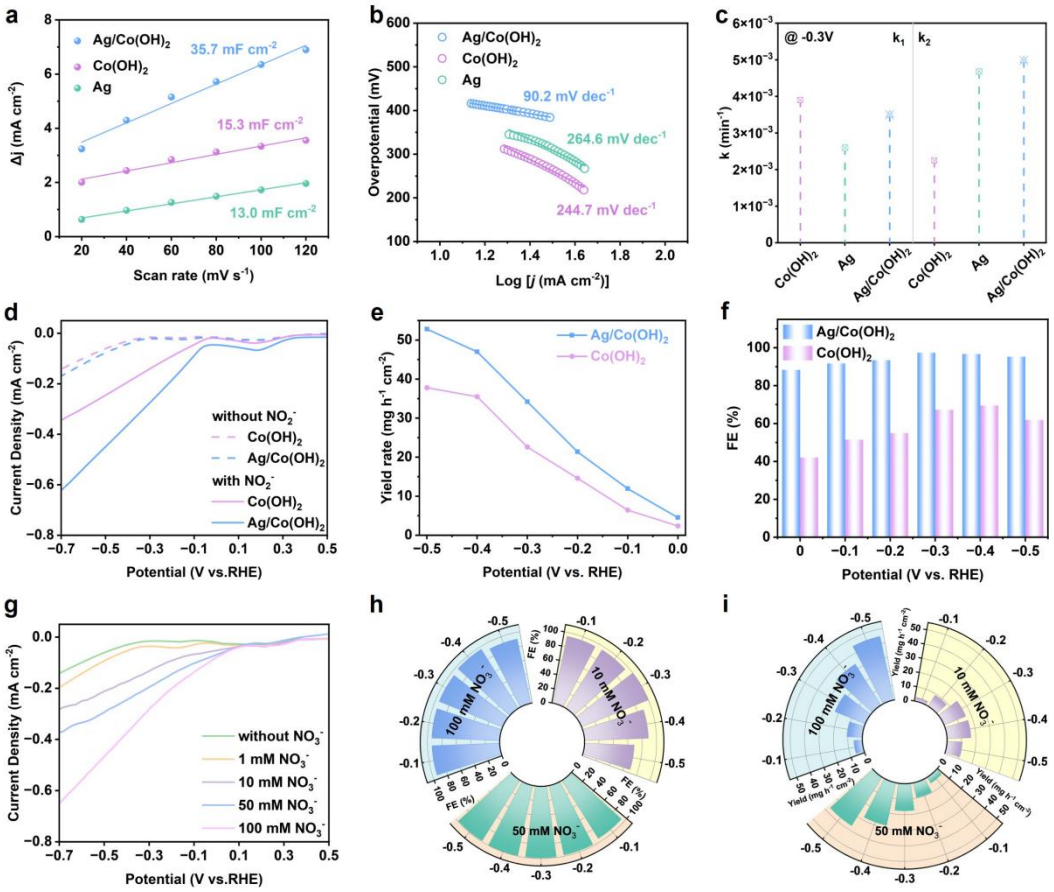

Figure 4. (**a**) C_{dl} curves and (**b**) Tafel plots of Ag, $Co(OH)_2$, and $Ag/Co(OH)_2$. (**c**) Comparison of the kinetic rate constants (k values). (**d**) LSV curves, (**e**) NH_3 yields, and (**f**) Faradaic efficiencies for the NO_2RR over $Ag/Co(OH)_2$ and $Co(OH)_2$. (**g**) LSV curves at different nitrate concentrations. (**h**) Faradaic efficiencies and (**i**) NH_3 yields in nitrate electrolytes with different concentrations.

To track the dynamic electronic evolution of the catalyst during nitrate reduction, we performed *in-situ* XANES characterization under varying applied potentials. Figures 5a and S16 display the Ag K-edge *in-situ* XANES spectra acquired for $Ag/Co(OH)_2$ at different potentials. As the applied potential was shifted from the open-circuit potential (OCP) toward −0.4 V vs. RHE, the Ag absorption edge gradually shifted toward lower energy, demonstrating the partial electron loss of Ag species [52]. Apparently, the Ag-O and Ag-Ag shell displayed an obvious dynamic change during NO_3RR. Quantitative analysis using the Ag oxidation state calibration curve in Figures 5b and S18 revealed that the average oxidation state of Ag continuously increased with increasing cathodic polarization, confirming that the valence state of Ag can be dynamically controlled by potential. Figures 5c and S17 present the Co K-edge *in-situ* XANES spectra at different potentials; the Co absorption edge likewise shifted toward lower energy during the potential reduction, indicating reduction of Co sites [53]. Similarly, the Co-O and Co-Co shell displayed an obvious dynamic change during NO_3RR. Based on the Co oxidation state calibration curve in Figures 5d and S19, the average oxidation state of Co progressively declined with cathodic polarization, demonstrating that Co sites participate in the electron transfer during nitrate reduction. These *in-situ* XAFS results collectively confirm that under cathodic polarization conditions for NO_3^- reduction, both Ag and Co sites undergo reversible valence-state reconstruction, and the dynamically evolving mixed-valence Ag-Co sites synergistically drive the electroreduction of nitrate. The WT-EXAFS further elucidates the differentiated structural evolution of Ag and Co sites. In contrast, the Co–O coordination in the $Co(OH)_2$ framework remained essentially unchanged [54]. These findings indicate that Ag serves as a potential-responsive active site, whereas $Co(OH)_2$ functions as a stabilizing support (Figures S20 and S21).

In-Situ electrochemical impedance spectroscopy (EIS) was employed to investigate the interfacial kinetics of the catalysts. As shown in the Nyquist plots at −0.3 V, $Ag/Co(OH)_2$ exhibits a much smaller charge-transfer resistance (R_{ct}) than those of Ag and $Co(OH)_2$, demonstrating accelerated electron transfer across the heterointerface (Figure S22). The subsequent Bode plots provide strong evidence for the key role of hydrogen species in the nitrate reduction reaction mechanism (Figures 5e,f and S23) [55]. During the HER, at relatively mild potentials, the phase angle is mainly distributed in the low-to-intermediate frequency range (1–10 Hz), which can

be associated with the sluggish Volmer step for *H generation ($H_2O + M + e^- \rightarrow M–H + OH^-$). At more negative potentials, the phase-angle response shifts toward the intermediate-to-high frequency range (10–100 Hz) with a decreased intensity, suggesting that the generated *H is consumed through the Heyrovsky step to produce H_2 [56]. However, upon introducing nitrate (NO_3^-), the phase-angle response changes markedly and shifts toward a higher-frequency region even at relatively low overpotentials. This behavior indicates that the generated H species are efficiently consumed by the nitrate reduction reaction rather than participating in the competing HER [57]. Such efficient utilization of H species highlights the excellent capability of Ag/$Co(OH)_2$ to promote selective ammonia synthesis while suppressing the competing HER. In the presence of NO_3^-, the charge-transfer resistance is also substantially reduced, further confirming the favorable electron-transfer kinetics of the catalyst and suggesting a dynamic balance between *H generation and its consumption by nitrate-derived species [58]. The *in-situ* EIS results demonstrate that the unique electronic structure and surface properties of Ag/$Co(OH)_2$ enable efficient *H-mediated hydrogenation of the NO_2^- intermediate, thereby enhancing the overall NO_3RR kinetics and ammonia selectivity.

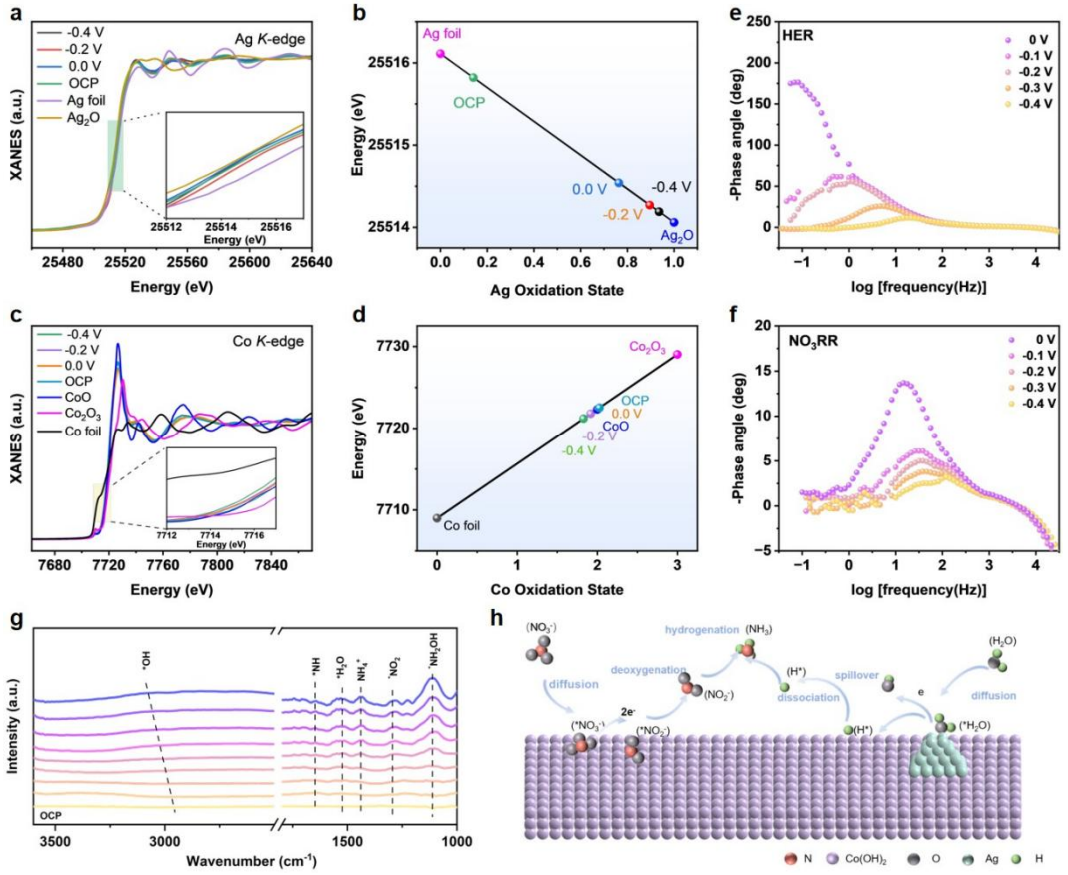

Figure 5. (**a**) Ag K-edge *in-situ* XANES spectra and (**b**) corresponding Ag oxidation-state calibration of Ag/$Co(OH)_2$ collected at different applied potentials. (**c**) Co K-edge *in-situ* XANES spectra and (**d**) corresponding Co oxidation-state calibration of Ag/$Co(OH)_2$ at varied potentials. *In-Situ* Bode phase plots of Ag/$Co(OH)_2$ recorded in (**e**) nitrate-free electrolyte (HER condition) and (**f**) nitrate-containing electrolyte (NO_3RR condition) under different potentials. (**g**) Potential-dependent *in-situ* FTIR spectra of Ag/$Co(OH)_2$ for NO_3RR. (**h**) Schematic illustration of the proposed tandem electrocatalytic NO_3^--to-NH_3 reaction mechanism over Ag/$Co(OH)_2$ catalyst.

In-Situ Fourier transform infrared spectroscopy (*in-situ* FTIR) was further performed to investigate the reaction mechanism of NO_3RR. This operando characterization provides direct information on reaction intermediates and enables their identification at the molecular level. The positive and negative FTIR signals correspond to the formation and consumption of surface species, respectively. As shown in Figures 5g and S24, four distinct absorption features are observed in the FTIR spectra of Ag/$Co(OH)_2$. The band observed at 1274 cm^{-1}, ascribed to the N–O asymmetric stretching vibration of NO_2, exhibits a gradual increase in intensity with increasingly negative applied potentials, corroborating the reduction of NO_3^- to NO_2^- during the NO_3RR [59–61]. An upward band at 1110 cm^{-1} is associated with the N–O stretching vibration of NH_2OH, which is considered a key intermediate in the NO_2RR pathway [62,63]. The upward band at 1444 cm^{-1}, associated with NH_4^+ and becomes progressively stronger at more negative potentials, indicating the formation of NH_3 [64]. Furthermore, the absorption band at approximately

1630 cm^{-1} is attributed to the H–O–H bending vibration of interfacial water molecules, reflecting changes in the interfacial water environment under cathodic polarization [65].

The peak can be assigned to the σ (N–H) bending stretching mode of NH_x species. The broad absorption band within the 3400–3200 cm^{-1} range can be attributed to the O-H stretching vibration of adsorbed H_2O. The three-dimensional FTIR spectra (Figure S25) provide a visual representation of the temporal evolution of the detected species. The rapid attenuation of the characteristic surface signals on Ag/$Co(OH)_2$, accompanied by a simultaneous increase in the signal associated with the hydrogenation intermediate *NH_2, confirms that the Ag nanoparticles substantially promote the generation of reactive hydrogen species. Figure 5h shows the proposed tandem electrocatalytic NO_3^--to-NH_3 mechanism of Ag/$Co(OH)_2$. The surface Ag nanoparticles combined with the $Co(OH)_2$ substrate, serving as the preferential adsorption site for nitrate, generate a synergistic catalytic effect and effectively lower the energy barrier for the subsequent hydrogenation step.

To further explore the potential of the as-prepared catalyst for practical energy-conversion applications, a Zn–NO_3^- battery was assembled using Ag/$Co(OH)_2$ as the cathode and Zn foil as the anode, and its electrochemical performance was preliminarily evaluated. This system not only enables the catalytic reduction of nitrate but also generates electricity simultaneously, integrating wastewater treatment with energy recovery. As shown in Figure 6a, the battery delivers a stable open-circuit voltage of 1.258 V. The discharge polarization and power density curves (Figure 6b) show a typical trend, with the power density initially increasing and then decreasing as the discharge current density increases. A maximum power density of 5.8 mW cm^{-2} is achieved at a current density of approximately 18 mA cm^{-2}, demonstrating the good power output capability of the Zn–NO_3^- battery. The battery also exhibits excellent rate performance under varying loads. As shown in Figure 6c, relatively stable discharge voltage plateaus are maintained at stepwise current densities of 1, 5, 10, 15, and 20 mA cm^{-2}. Notably, when the current density is switched back to 1 mA cm^{-2}, the cell voltage rapidly recovers to its initial level and remains stable, indicating the good structural stability of the Ag/$Co(OH)_2$ NWs cathode under different discharge loads. Finally, a long-term galvanostatic discharge test was conducted (Figure 6d). During continuous operation for 15 h, the discharge voltage remains relatively stable without obvious voltage decay or cell failure, confirming the excellent durability of the assembled device.

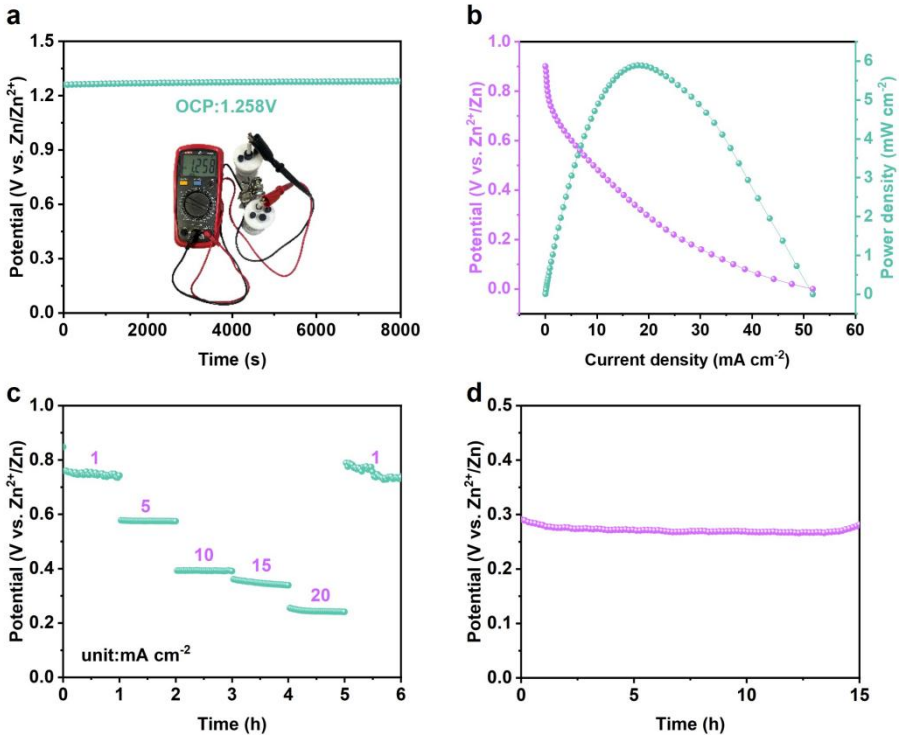

Figure 6. Zn–NO_3^- battery assembled using the Ag/$Co(OH)_2$ catalyst. (**a**) Open-circuit voltage. (**b**) Polarization curve and corresponding power density. (**c**) Discharge voltages at different current densities. (**d**) Long-term electrochemical stability tests.

4. Conclusions

This study successfully develops an Ag/$Co(OH)_2$ heterostructure catalyst composed of Ag nanoparticles and $Co(OH)_2$ nanowires, and systematically elucidates its structure–activity relationship for the highly efficient

electrocatalytic reduction of nitrate for ammonia production. Mechanistic studies demonstrate that $Co(OH)_2$ primarily facilitates the adsorption and initial activation of NO_3^-, promoting its conversion to NO_2^-; whereas the Ag nanoparticles serve as highly efficient hydrogenation sites, facilitating the generation of *H at the interface and accelerating the subsequent deep hydrogenation process. The two components achieve functional complementarity through the heterointerface, effectively optimizing the multi-step reaction pathway and the kinetic behavior. Benefiting from this synergistic mechanism, the $Ag/Co(OH)_2$ NWs achieve a 96.35% ammonia Faradaic efficiency at −0.4 V (vs. RHE) and maintain a Faradaic efficiency exceeding 80% over a broad potential range of 0.1–−0.7 V, demonstrating outstanding catalytic activity, selectivity, and broad potential applicability. This work not only provides an effective heterostructured catalyst for the high-efficiency electrocatalytic synthesis of ammonia under ambient conditions but also offers an important theoretical foundation and material design strategy for the synergistic design of adsorption and hydrogenation sites in multi-electron electrochemical reduction reactions.

Supplementary Materials

The additional data and information can be downloaded at: https://media.sciltp.com/articles/others/26112011 11085910/eChem-26100094-SI.pdf. References [66–73] are cited in the Supplementary Materials.

Author Contributions

L.Z.: Writing—original draft, project administration, funding acquisition. Y.L.: Investigation, formal analysis, data curation. Q.B.: Investigation, data curation, characterization. R.L.: Formal analysis. H.S.: Supervision, funding acquisition. All authors have read and agreed to the published version of the manuscript.

Funding

This work was sponsored by Natural Science Foundation of Henan (252300421175), National Natural Science Foundation of China (Grants No. 92580136, 22675270, and 22605335). This work was supported by the Postdoctoral Fellowship Program of CPSF under Grant Number GZC20260661.

Informed Consent Statement

Informed consent was obtained from all individual participants included in the study. Consent to publish was obtained from all individual participants included in this study.

Data Availability Statement

All the necessary data are available in the main text and Supplementary Materials. The data are also available on request from the authors.

Acknowledgments

The authors thank the Center for Advanced Analysis and Gene Sequencing of Zhengzhou University and High energy photon source for help with characterizations.

Conflicts of Interest

The authors declare no conflict of interest.

Use of AI and AI-Assisted Technologies

AI-assisted tools were used solely for language editing and improving manuscript readability. All scientific work, data analysis, interpretations, and conclusions were independently conducted and verified by the authors, who take full responsibility for the manuscript.

References

1. Zheng, M.; Wan, Y.; Huang, Z.H.; et al. Interfacial Synergistic Hydrogen Spillover and Electron Transfer for Boosting Electrocatalytic Nitrate Reduction to Ammonia. *Adv. Mater.* **2026**, *38*, e14834. https://doi.org/10.1002/adma.202514834.
2. Xu, M.; Wang, R.; Wang, Z.; et al. Hydroxyl-Rich Nanocavities on Perovskite Enable Nearly Barrierless Intramolecular Hydrogen Transfer for Nitrate Electroreduction to Ammonia. *Nat. Commun.* **2026**, *17*, 4128. https://doi.org/10.1038/s41467-026-74405-1.

3. Zuo, Y.; Sun, M.; Li, T.; et al. Capturing Copper Single Atom in Proton Donor Stimulated O-End Nitrate Reduction. *Adv. Mater.* **2025**, *37*, 2415632. https://doi.org/10.1002/adma.202415632.
4. Tang, H.; Ding, J.; Feng, Z.; et al. Ligand-Directed Nitrate Incorporation into Reconstructed Oxyhydroxides for Durable Seawater Electrolysis. *Angew. Chem. Int. Ed.* **2026**, *65*, e3751410. https://doi.org/10.1002/anie.3751410.
5. Chen, D.; Guo, Z.; Wang, J.; et al. Lattice-Engineered Dual-Electron-Drive Electrode for Selective Ammonia Production from Nitrate. *Adv. Mater.* **2026**, *38*, e73699. https://doi.org/10.1002/adma.73699.
6. Song, S.; Tayyebi, A.; Tayebi, M.; et al. Advancing Tandem Organic Solar Cells with Ternary Acceptor Control for High-Power Modules and Solar-to-Ammonia Conversion. *Adv. Funct. Mater.* **2026**, *36*, e76326. https://doi.org/10.1002/adfm.76326.
7. Zhang, W.; Guo, F.; Gong, W.; et al. Electrochemical Shortcut Denitrification Coupled with Chemical Diazotization for Low-Carbon Nitrate Wastewater Treatment. *Angew. Chem. Int. Ed.* **2026**, *65*, e16226. https://doi.org/10.1002/anie.202516226.
8. Huang, L.; Zhang, P.; Ge, X.; et al. Efficient Neutral Nitrate-to-Ammonia Electrosynthesis Using Synergistic Ru-Based Nanoalloys on Nitrogen-Doped Carbon. *Nano-Micro Lett.* **2026**, *18*, 66. https://doi.org/10.1007/s40820-025-01896-w.
9. Xia, H.; Lan, H.; Yu, Y.; et al. Spin State and Orbital Engineering of Cuprous Oxide for Efficient Nitrate Reduction. *Nat. Commun.* **2026**, *17*, 9827. https://doi.org/10.1038/s41467-026-76420-8.
10. Chen, X.; Yi, J.; Ding, G.; et al. Regulating Interfacial Water Structure on CoNi/MoN Heterostructures Boosts Electrocatalytic Nitrate Reduction to Ammonia. *Carbon Energy* **2026**, *8*, e70320. https://doi.org/10.1002/cey2.70320.
11. Choi, J.H.; Lee, H.H.; Jeong, J.H.; et al. Electrochemical Design of Atomically Conformal Ga_2O_3 Buffer Layers via Cu_2O-Catalyzed Nitrate Reduction Reaction for Efficient Cu_2O Photocathodes. *Carbon Energy* **2026**, *8*, e70226. https://doi.org/10.1002/cey2.70226.
12. Ma, Z.; Yang, T.; Huang, J.; et al. Enhanced electrocatalytic reduction of nitrate to ammonia via anchoring CuNi alloy on oxygen vacancy-rich N-$Ti_3C_2T_x$. *J. Mater. Sci. Technol.* **2025**, *233*, 193–200. https://doi.org/10.1016/j.jmst.2025.01.047.
13. Liu, Y.; Wei, J.; Yang, Z.; et al. Efficient tandem electroreduction of nitrate into ammonia through coupling Cu single atoms with adjacent Co_3O_4. *Nat. Commun.* **2024**, *15*, 3619. https://doi.org/10.1038/s41467-024-48035-4.
14. Zhao, X.; Wang, C.; Liu, S.; et al. An Ambient Photocatalytic Approach to *In-Situ* Prepare Cobalt/Cobalt Phosphide and Cobalt/Cobalt Phosphide@Graphene Heterojunction Nanomaterials with Optimized Charge Separation Effects for Highly Efficient Relayed Electrocatalytic NO_x—Reduction to NH_3. *Carbon Energy* **2026**, *8*, e70248. https://doi.org/10.1002/cey2.70248.
15. Chang, G.; Chen, X.; Lv, J.J.; et al. Cobalt-Based Electrocatalysts for Sustainable Nitrate Conversion: Structural Design and Mechanistic Advancements. *Nano-Micro Lett.* **2026**, *18*, 73. https://doi.org/10.1007/s40820-025-01877-z.
16. Jiang, L.; Bai, X.; Zhi, X.; et al. New Mechanistic Insights into Electrokinetic Competition between Nitrogen Reduction and Hydrogen Evolution Reactions. *Adv. Energy Mater.* **2024**, *14*, 2303809. https://doi.org/10.1002/aenm.202303809.
17. Lu, J.; Wang, H.; Mou, Y.; et al. Synergistic Catalysis in Electrocatalytic Nitrate Reduction. *eChem* **2026**, *2*, 4. https://doi.org/10.53941/echem.2026.100004.
18. Xu, J.; Liu, H.; Zhang, S.; et al. Integrated Cascade Catalysts for Electrochemical Nitrate Reduction to Ammonia. *J. Am. Chem. Soc.* **2026**, *148*, 148–161. https://doi.org/10.1021/jacs.5c03265.
19. Tayyebi, A.; Juyeon, J.; Moghaddam, M.H.; et al. High-Performance and Stable NH_3 Production Using a TiO_2-Protected Si Photocathode and Patterned Au Loading. *EES Catal.* **2025**, *3*, 446–458. https://doi.org/10.1039/d4ey00282b.
20. Zhang, Y.; Wang, C.; Liu, Y.; et al. Highly dispersed Cu/WO_3 heterojunctions featured by promoting hydrogen radical-mediated pathway for efficient nitrate reduction to ammonia. *Sci. China Mater.* **2025**, *68*, 4498–4506. https://doi.org/10.1007/s40843-025-3480-1.
21. Yue, H.; Xie, W.; Wan, D.; et al. Tuning Intermediate Adsorption and Interfacial Water Networks via Lattice Strain of NiFe Alloys Boosts Low-Concentration Nitrate Electroreduction. *Adv. Mater.* **2026**, *38*, e73761. https://doi.org/10.1002/adma.73761.
22. Chen, X.; Wang, X.; Le, J.; et al. Revealing the Role of Interfacial Water and Key Intermediates at Ruthenium Surfaces in the Alkaline Hydrogen Evolution Reaction. *Nat. Commun.* **2023**, *14*, 5289. https://doi.org/10.1038/s41467-023-41030-1.
23. Luo, Z.; Guo, Y.; Qian, Y.; et al. Synergistic M-O Dual-Atom Pairs Induced Interfacial Water Hydrogen Bonding Network for Boosting $MoSe_2$ Electrocatalytic Performance. *Adv. Funct. Mater.* **2024**, *34*, 2405881. https://doi.org/10.1002/adfm.202405881.
24. Zhang, Z.; Sun, Z.; Wei, Z.; et al. Rational Design of Nano and Atomically Dispersed Catalysts for Electrocatalytic Ammonia Synthesis from Nitrate. *eChem* **2025**, *1*, 2. https://doi.org/10.53941/echem.2025.100002.
25. Zhang, Z.; Liu, M.; Ge, B.; et al. *In-Situ* reconstructed Cu/NiO nanosheets synergistically boosting nitrate electroreduction to ammonia. *Chin. Chem. Lett.* **2025**, *36*, 110657. https://doi.org/10.1016/j.cclet.2024.110657.
26. Wang, X.; Tang, S.; Wu, Q.; et al. Perspective on Modular Electrocatalysis for Carbon and Nitrogen Cycling. *Nano-Micro Lett.* **2026**, *18*, 373. https://doi.org/10.1007/s40820-026-02231-7.

27. Guo, Q.; Han, T.; Zheng, Y.; et al. Highly Selective Electrocatalytic Ammonia Synthesis Enabled by Spatial Separation of Active Hydrogen Capture and Spillover Sites. *Angew. Chem. Int. Ed.* **2026**, *65*, e5589616. https://doi.org/10.1002/anie.5589616.
28. Zhang, C.; Zhang, Y.; Deng, R.; et al. Enabling Logistics Automation in Nanofactory: Cobalt Phosphide Embedded Metal–Organic Frameworks for Efficient Electrocatalytic Nitrate Reduction to Ammonia. *Adv. Mater.* **2024**, *36*, 2313844. https://doi.org/10.1002/adma.202313844.
29. Gowdru, S.M.; Nagaraju, P.H.; Chen, Y.C.; et al. Enhanced electrocatalytic nitrate reduction to ammonia on silver nanocubes. *Chem. Commun.* **2025**, *61*, 6965–6968. https://doi.org/10.1039/d5cc01409c.
30. Tan, J.; Li, Y.; Qiao, L.; et al. Atomically Precise Ag_9Cu_6 and Ag_{15} Nanoclusters for Nitrate Electroreduction to NH_3: Probing the Cu Doping Effect. *eChem* **2026**, *2*, 6. https://doi.org/10.53941/echem.2026.100006.
31. Li, R.; Ma, R.; Zhang, L.L.; et al. Sulfur-Bridge Engineering Enables Reverse Hydrogen Spillover to Atomic Cu for Nitrate-to-Ammonia Electrocatalysis. *Angew. Chem. Int. Ed.* **2026**, *65*, e7688164. https://doi.org/10.1002/anie.7688164.
32. Ye, J.; Zhu, J.; Wang, A.; et al. Enhanced active hydrogen supply promotes interfacial tandem electrocatalytic nitrate reduction to ammonia. *J. Colloid Interface Sci.* **2026**, *707*, 139718. https://doi.org/10.1016/j.jcis.2025.139718.
33. Yan, W.; Mou, Y.; Li, M.; et al. C_{15}-Phase Platinum-Lanthanide Intermetallics for Efficient Hydrogen Evolution: Identifying Lanthanide's Enhanced Mechanism. *Adv. Mater.* **2025**, *37*, 2506936. https://doi.org/10.1002/adma.202506936.
34. Zhang, Y.; Zhang, W.; Zhang, X.; et al. Inducing Intermolecular Oxygen Coupling by Introducing S and FeOOH on $Co(OH)_2$ Nanoneedle Arrays for Industrial Water Oxidation. *Small* **2024**, *20*, 2405080. https://doi.org/10.1002/smll.202405080.
35. Xu, Y.; Sheng, Y.; Wang, M.; et al. Interface coupling induced built-in electric fields boost electrochemical nitrate reduction to ammonia over CuO@MnO_2 core–shell hierarchical nanoarrays. *J. Mater. Chem. A* **2022**, *10*, 16883–16890. https://doi.org/10.1039/d2ta02006h.
36. Wyss, V.; Dinu, I.A.; Marot, L.; et al. Thermocatalytic Epoxidation by Cobalt Sulfide Inspired by the Material's Electrocatalytic Activity for Oxygen Evolution Reaction. *Catal. Sci. Technol.* **2024**, *14*, 4550–4565. https://doi.org/10.1039/d4cy00518j.
37. Wang, W.; Wang, Y.; Qi, Y.; et al. Interfacial Electronic Modulation Redirects Anodic Radical Chemistry for Selective C–C Bond Cleavage in Electro-Oxidative Lignin Depolymerization. *Angew. Chem. Int. Ed.* **2026**, *65*, e1876863. https://doi.org/10.1002/anie.1876863.
38. Chen, W.; Sun, Z.; Zhen, S.; et al. Tuning Asymmetric S-Bridged Cu–Co Dual Sites at Atomic-Level for Efficient Ammonia Electrosynthesis. *Adv. Funct. Mater.* **2026**, *36*, e09200. https://doi.org/10.1002/adfm.202509200.
39. Wu, Z.; Shi, Z.; Xie, F.; et al. Tandem Catalysis Enables High-Rate Nitrate Electroreduction via Interfacial Water Regulation. *Adv. Mater.* **2026**, *38*, e72651. https://doi.org/10.1002/adma.72651.
40. Lian, Z.; Gao, F.; Xiao, H.; et al. Photo-self-Fenton Reaction Mediated by Atomically Dispersed Ag–Co Photocatalysts toward Efficient Degradation of Organic Pollutants. *Angew. Chem. Int. Ed.* **2024**, *63*, e202318927. https://doi.org/10.1002/anie.202318927.
41. Xu, S.; Li, J.; Cheng, J.; et al. Single atom–cluster synergy in Ag catalysts enables chiral glyceric acid from biomass. *Sci. Adv.* **2025**, *11*, eadz4136. https://doi.org/10.1126/sciadv.adz4136.
42. Bao, T.; Wu, Y.; Tang, C.; et al. A Full-Spectrum-Responsive MOF-on-MOF Heterojunction Photocatalyst for Concurrent Nitrate Reduction and Biomass Oxidation. *Angew. Chem. Int. Ed.* **2026**, *65*, e8582451. https://doi.org/10.1002/anie.8582451.
43. Long, Y.; Zhu, X.; Gao, C.; et al. Modulation of Co spin state at Co_3O_4 crystalline-amorphous interfaces for CO oxidation and N_2O decomposition. *Nat. Commun.* **2025**, *16*, 1048. https://doi.org/10.1038/s41467-025-56487-5.
44. Wen, M.; Yang, W.Y.; Zhang, Z.H.; et al. Co–Ag–Ce Triple-Phase Interface in Hollow Microreactor with Ag Single-Atom for Directing HMF Oxidation from HMFCA to FDCA. *ACS Catal.* **2026**, *16*, 17256–17274. https://doi.org/10.1021/acscatal.6c04372.
45. Zhang, L.; Cai, Y.; Li, Y.; et al. Unlocking high-current-density nitrate reduction and formaldehyde oxidation synergy for scalable ammonia production and fixation. *Energy Environ. Sci.* **2025**, *18*, 2804–2816. https://doi.org/10.1039/d4ee04382k.
46. Guo, X.; Gao, Y.; Zhang, C.; et al. Plasma-coupled electrochemical ammonia synthesis from air and water under ambient conditions. *Nat. Protoc.* **2026**, *21*, 4192–4216. https://doi.org/10.1038/s41596-026-01332-2.
47. Geng, J.; Wu, Y.; Ji, S. Laser-Programmed Spatial Relay Catalysis on Co–Ag Dual Heterojunctions for Efficient Nitrate-to-Ammonia Conversion via Migratory *NO_2 Shuttling. *Angew. Chem. Int. Ed.* **2025**, *64*, e202515393. https://doi.org/10.1002/anie.202515393.
48. Wang, Y.; Zhou, W.; Jia, R.; et al. Splicing the active phases of copper/cobalt-based catalysts achieves high-rate tandem electroreduction of nitrate to ammonia. *Nat. Commun.* **2022**, *13*, 2447. https://doi.org/10.1038/s41467-022-28728-4.
49. Zhang, W.; Jiao, D.; Liu, H.; et al. Atomic-site synergy in Ag-Co dual-metal-site photocatalyst steering highly selective NO-to-nitrate conversion with inhibiting NO_2 emission. *Appl. Catal. B Environ. Energy* **2026**, *384*, 126145. https://doi.org/10.1016/j.apcatb.2025.126145.
50. Wu, M.; Luo, J.; Qian, Q.; et al. Co–Ag Atomic Pairs Enable Localized Lattice Oxygen Activation for Stable Oxygen Evolution. *Adv. Funct. Mater.* **2026**, *36*, e21658. https://doi.org/10.1002/adfm.202521658.

51. Xie, F.; Kang, X.; Li, Z.; et al. Interfacial Confinement-Programmed Hydrogen Spillover on Ag/CoNiS Boosts Nitrate-to-Ammonia Electrosynthesis. *Adv. Mater.* **2026**, *38*, e73885. https://doi.org/10.1002/adma.73885.
52. Huang, H.; Zhang, Y.; Chen, W.; et al. Dynamic Stabilization of $Cu^{\delta+}$ in Heterostructured Ag_0-$CuAgO_x$ for High-Performing Nitrate Electroreduction. *Adv. Energy Mater.* **2025**, *15*, 2405534. https://doi.org/10.1002/aenm.202405534.
53. Mei, W.; Chang, C.W.; Li, Z.; et al. Robust Oxygen-Vacancy-Engineered $Co(OH)_2$/Cu Heterostructures Boost Nitrate Electroreduction to Ammonia beyond 2 A cm^{-2}. *Adv. Mater.* **2025**, *37*, 2507363. https://doi.org/10.1002/adma.202507363.
54. Sun, F.; Ni, C.; Zhang, Y.; et al. Operando Imaging of Adsorbate-Charge Cooperative Reconstruction into Terminal Active Co–OH Sites. *J. Am. Chem. Soc.* **2026**, *148*, 23208–23219. https://doi.org/10.1021/jacs.6c06054.
55. Wang, Y.; Cheng, Y.; Gao, M.; et al. Modulating Hydrogen Species for Efficient and Sustainable Nitrate Electroreduction to Ammonia. *Angew. Chem. Int. Ed.* **2026**, *65*, e24803. https://doi.org/10.1002/anie.202524803.
56. Li, Y.; Lu, Z.; Zheng, L.; et al. The Synergistic Catalysis Effect on Electrochemical Nitrate Reduction at the Dual-Function Active Sites of the Heterostructure. *Energy Environ. Sci.* **2024**, *17*, 4582–4593. https://doi.org/10.1039/d4ee00784k.
57. Zuo, M.; Kong, Y.; Zhou, H.; et al. *In Situ* Exsolution to Form Cu Nanoparticles on Cu–Doped $LaFeO_3$ Perovskite Oxides for Efficient Electrocatalytic Reduction of Nitrate to Ammonia. *Adv. Funct. Mater.* **2026**, *36*, e13364. https://doi.org/10.1002/adfm.202513364.
58. Zhou, P.; Lv, X.; Huang, H.; et al. Construction of Ag–$Co(OH)_2$ Tandem Heterogeneous Electrocatalyst Induced Aldehyde Oxidation and the Co-Activation of Reactants for Biomass Effective and Multi-Selective Upgrading. *Adv. Mater.* **2024**, *36*, 2312402. https://doi.org/10.1002/adma.202312402.
59. Xiao, Y.; Tan, X.; Du, B.; et al. Strained Au skin on Mesoporous Intermetallic $AuCu_3$ Nanocoral for Electrocatalytic Conversion of Nitrate to Ammonia across a Wide Concentration Range. *Angew. Chem. Int. Ed.* **2024**, *63*, e202408758. https://doi.org/10.1002/anie.202408758.
60. Chen, Z.; Liu, G.; Zhao, Y.; et al. Co_1Zn Single-Atom Alloy Boosts Active Hydrogen Spillover for Highly Efficient Electrosynthesis of Ammonia over 2 A cm^{-2} Current Density. *Angew. Chem. Int. Ed.* **2026**, *65*, e23740. https://doi.org/10.1002/anie.202523740.
61. Yu, L.; Mu, J.; Liu, H.; et al. *In Situ* Reconstructed Bi_0-Guided Electron-Deficient $Co(OH)_2$ for Enhanced Electrocatalytic Nitrate Reduction to Ammonia. *Adv. Funct. Mater.* **2025**, *35*, 2424119. https://doi.org/10.1002/adfm.202424119.
62. Wei, Y.; Huang, J.; Chen, H.; et al. Electrocatalytic Nitrate Reduction on Metallic CoNi-Terminated Catalyst with Industrial-Level Current Density in Neutral Medium. *Adv. Mater.* **2024**, *36*, 2404774. https://doi.org/10.1002/adma.202404774.
63. Tang, Y.; Jiang, Z.; Yuan, Y.; et al. Selective electrosynthesis of hydroxylamine from aqueous nitrate/nitrite by suppressing further reduction. *Nat. Commun.* **2024**, *15*, 9800. https://doi.org/10.1038/s41467-024-54204-2.
64. Gao, W.; Xie, K.; Xie, J.; et al. Alloying of Cu with Ru Enabling the Relay Catalysis for Reduction of Nitrate to Ammonia. *Adv. Mater.* **2023**, *35*, 2202952. https://doi.org/10.1002/adma.202202952.
65. Chen, X.; Cheng, Y.; Zhang, B.; et al. Gradient-Concentration RuCo Electrocatalyst for Efficient and Stable Electroreduction of Nitrate into Ammonia. *Nat. Commun.* **2024**, *15*, 6278. https://doi.org/10.1038/s41467-024-50670-w.
66. Fan, Z.; Cao, C.; Yang, X.; et al. Interfacial Electronic Interactions Promoted Activation for Nitrate Electroreduction to Ammonia over Ag-Modified Co_3O_4. *Angew. Chem. Int. Ed.* **2024**, *63*, e202410356. https://doi.org/10.1002/anie.202410356.
67. Dong, H.; Ye, J.; Liu, X.; et al. Spatially Separated Ag@Cu_3N Tandem Electrocatalyst with High Nitrate-to-Ammonia Selectivity via Decoupled Deoxygenation-Hydrogenation Pathway. *Adv. Funct. Mater.* **2026**, *36*, e202526882. https://doi.org/10.1002/adfm.202526882.
68. Feng, Z.; He, Y.; Cui, Y.; et al. Efficient Tandem Electrocatalytic Nitrate Reduction to Ammonia on Bimodal Nanoporous Ag/Ag–Co across Broad Nitrate Concentrations. *Nano Lett.* **2024**, *24*, 11929–11936. https://doi.org/10.1021/acs.nanolett.4c03218.
69. Zhang, Y.; Ma, J.; Wang, B.; et al. Aldehyde Directed *In Situ* Loading of Ag Nanodots Around the Open Metal Sites of MOFs for the Tandem Catalysis of Nitrate to Ammonia. *Small* **2025**, *21*, 2408602. https://doi.org/10.1002/smll.202408602.
70. Liu, X.; Xiang, T.; Liu, J.; et al. Ag Single Atoms Boosting Water Dissociation on Cu Nanowires for Efficient H*-Mediated Nitrate Reduction at Ultra-Low Concentrations with Ammonia Recovery. *Adv. Funct. Mater.* **2026**, *36*, e21402. https://doi.org/10.1002/adfm.202521402.
71. Zhang, J.; He, W.; Quast, T.; et al. Single-entity Electrochemistry Unveils Dynamic Transformation during Tandem Catalysis of Cu_2O and Co_3O_4 for Converting NO^{3-} to NH_3. *Angew. Chem. Int. Ed.* **2023**, *62*, e202214830. https://doi.org/10.1002/anie.202214830.
72. Ren, Z.; Shi, K.; Meng, Z.; et al. Complete Single-Pass Conversion of Dilute Nitrate to Ammonia Using Cu/$Co(OH)_2$ Tandem Electrocatalyst. *ACS Energy Lett.* **2024**, *9*, 3849–3858. https://doi.org/10.1021/acsenergylett.4c01247.
73. Wu, S.; Jiang, Y.; Luo, W.; et al. Ag-Co_3O_4-CoOOH-Nanowires Tandem Catalyst for Efficient Electrocatalytic Conversion of Nitrate to Ammonia at Low Overpotential via Triple Reactions. *Adv. Sci.* **2023**, *10*, 2303789. https://doi.org/10.1002/advs.202303789.